This is an open access article published under an ACS AuthorChoice License, which permits copying and redistribution of the article or any adaptations for non-commercial purposes.

ACS OMEGA

Article

Cite This: ACS Omega 2020, 5, 104−112

http://pubs.acs.org/journal/acsodf

Crystal Chemistry, Band-Gap Red Shift, and Electrocatalytic Activity of Iron-Doped Gallium Oxide Ceramics

Bandi Mallesham,[†] Swadipta Roy,[†,‡,∥] Saptasree Bose,[§] Aruna N. Nair,[§] Sreeprasad Sreenivasan,[§] Vaithiyalingam Shutthanandan,[∥] and Chintalapalle V. Ramana*[,†]

[†]Center for Advanced Materials Research (CMR), [‡]Department of Metallurgical, Materials and Biomedical Engineering and [§]Department of Chemistry and Biochemistry, University of Texas at El Paso, 500 W University Ave, El Paso, Texas 79968, United States

[∥]Environmental Molecular Sciences Laboratory (EMSL), Pacific Northwest National Laboratory (PNNL), Richland, Washington 99352, United States

ABSTRACT: This work for the first time unfurls the fundamental mechanisms and sets the stage for an approach to derive electrocatalytic activity, which is otherwise not possible, in a traditionally known wide band-gap oxide material. Specifically, we report on the tunable optical properties, in terms of wide spectral selectivity and red-shifted band gap, and electrocatalytic behavior of iron (Fe)-doped gallium oxide (β-Ga_2O_3) model system. X-ray diffraction (XRD) studies of sintered $Ga_{2-x}Fe_xO_3$ (GFO) ($0.0 \le x \le 0.3$) compounds provide evidence for the Fe^{3+} substitution at Ga^{3+} site without any secondary phase formation. Rietveld refinement of XRD patterns reveals that the GFO compounds crystallize in monoclinic crystal symmetry with a $C2/m$ space group. The electronic structure of the GFO compounds probed using X-ray photoelectron spectroscopy data reveals that at lower concentrations, Fe exhibits mixed chemical valence states (Fe^{3+}, Fe^{2+}), whereas single chemical valence state (Fe^{3+}) is evident for higher Fe content (x = 0.20−0.30). The optical absorption spectra reveal a significant red shift in the optical band gap with Fe doping. The origin of the significant red shift even at low concentrations of Fe (x = 0.05) is attributed to the strong sp−d exchange interaction originated from the $3d^5$ electrons of Fe^{3+}. The optical absorption edge observed at ≈450 nm with lower intensity is the characteristic of Fe-doped compounds associated with Fe^{3+}−Fe^{3+} double-excitation process. Coupled with an optical band-gap red shift, electrocatalytic studies of GFO compounds reveal that, interestingly, Fe-doped Ga_2O_3 compound exhibits electrocatalytic activity in contrast to intrinsic Ga_2O_3. Fe-doped samples (GFO) demonstrated appreciable electrocatalytic activity toward the generation of H_2 through electrocatalytic water splitting. An onset potential and Tafel slope of GFO compounds include ∼900 mV, ∼210 mV dec^{-1} (x = 0.15) and ∼1036 mV, ∼290 mV dec^{-1} (x = 0.30), respectively. The electrocatalytic activity of Fe-doped Ga-oxide compounds is attributed to the cumulative effect of different mechanisms such as doping resulting in new catalytic centers, enhanced conductivity, and electron mobility. Hence, in this report, for the first time, we explored a new pathway; the electrocatalytic behavior of Fe-doped Ga_2O_3 resulted due to Fe chemical states and red shift in the optical band gap. The implications derived from this work may be applicable to a large class of compounds, and further options may be available to design functional materials for electrocatalytic energy production.

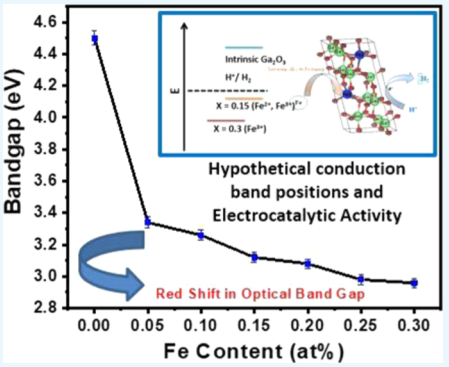

INTRODUCTION

Gallium oxide (β-Ga_2O_3) has been extensively explored in recent years due to its viable applications in modern optical, electronic, and optoelectronic devices such as solar-blind UV photodetectors, power electronics, solar cells, phosphors, transparent conducting electrode coatings, and optoelectronic devices.[1−5] Ga_2O_3 exhibits deep optical transparency in the ultraviolet (UV) region; hence, it is considered as a promising candidate for next-generation deep UV photodetectors.[6,7] Moreover, compared to conventional semiconductors such as SiC and GaN, β-Ga_2O_3 exhibits high break downfield (8 MV/cm) and higher Baliga's figures of merit (≈3000), which makes it suitable for power electronic device applications.[8] β-Ga_2O_3 is also known for excellent chemical sensing, where the functionality is reported toward a variety of gases such as O_2, H_2, CH_4, and CO.[9−13] Due to the presence of oxygen vacancies, its electrical conductivity changes upon the adsorption of these gas molecules. Ga_2O_3 is a promising oxygen sensing material at high temperatures; the oxygen sensing ability is attributed to its n-type semiconducting nature and excellent chemical and thermal stabilities at high temperatures.[14−16] In addition, Ga_2O_3 shows the magnetic memory effect even above room temperature due to the presence of conduction electron spins.[17,18] In view of these properties and phenomena, Ga_2O_3 grabs the recent attention of researchers, while the fundamental understanding of the

Received: May 31, 2019
Accepted: September 10, 2019
Published: December 27, 2019

Downloaded via PACIFIC NORTHWEST NATL LABORATORY on January 21, 2020 at 18:49:13 (UTC).
See https://pubs.acs.org/sharingguidelines for options on how to legitimately share published articles.

© 2019 American Chemical Society

DOI: 10.1021/acsomega.9b01604
ACS Omega 2020, 5, 104−112

mechanisms and functional properties so as to fully utilize the potential of the Ga_2O_3-based materials in emerging technological applications is the primary driving factor.

Ga_2O_3 exhibits five different types of polymorphs: corundum (α), monoclinic (β), defective spinel (γ), orthorhombic (ε), and δ phase (also stabilizes orthorhombic phase). Among these, monoclinic β-Ga_2O_3 was thermodynamically more stable than other phases.[19,20] While β-Ga_2O_3 can be fabricated in thin film and single crystal forms, doping of various elements in thin film and bulk β-Ga_2O_3 has been attempted to tailor the functional properties.[21] To alter the electronic structure and to derive new and unexpected optical, magnetic, electrical, catalytic, and optoelectronic properties, doping and alloying with selectively chosen elements is an efficient and proven method. For instance, it has been reported that the Sn- and Cr-doped β-Ga_2O_3 nanowires exhibit excellent luminescence properties suitable for display device applications.[22] Metal-doped Ga_2O_3 has been found to be attractive and exhibits superior photocatalytic activity for application in energy-harvesting devices. Enhanced photocatalytic activity has been observed in Ga_2O_3 by the approach of metal-ion dopants such as Ni, Zn, and Pb.[23−25] Recently, Zadeh et al. reported efficient photocatalytic activity in hexagonal α-Ga_2O_3 nanoflakes due to band narrowing.[26] The changes induced in optical absorption spectra and its consequent effect on band gap have been studied by doping different ions, namely, Cu, W, Ti, and Mo into Ga_2O_3.[27−30]

Tuning the optical and optoelectronic properties of Ga_2O_3 has gained great attention due to their potential integration into several technological applications, which include solar-blind photodetectors, photocatalysis, luminescent phosphors, and photovoltaics. Ga_2O_3 valance band edge is found to be located at −7.75 eV vs vacuum; hence, it can provide photogenerated charges with high oxidizing potentials, which makes it useful for photocatalytic applications.[24] In fact, Ga_2O_3 has been reported to be an excellent water-splitting photocatalyst for the generation of hydrogen. However, the main drawback associated with photocatalytic applications of Ga_2O_3 is its wide band gap (∼5 eV), which limits their functionality due to UV-only absorption. Thus, despite its greatest potential, in a broader context, the photocatalytic applications of this material are considerably limited because it fails to generate sufficient electron−hole pairs upon solar light illumination. Different approaches have been adopted to enhance the photocatalytic activity of Ga_2O_3-based materials. Doping with suitable ions is one of the most popular methods, where the photocatalytic properties of β-Ga_2O_3 were significantly altered by dopants. However, during the last few years, hydrogen (H_2) has been advocated as a clean and sustainable source of energy and is considered as an ideal candidate to meet the future energy requirements. Among different techniques available, electrocatalytic water splitting is considered the most economical and viable process. Electrocatalysts minimize the energy requirement for water splitting and, in this regard, platinum (Pt) shows the best result. However, the high price and low abundance of Pt limit its extensive use. As an alternative, sulfide-, phosphide-, and oxide-based materials have already been explored as an electrocatalyst. In the present work, for the first time, we report on the iron (Fe)-doping-facilitated selectivity across a wide spectral range and, specifically, the red-shifted optical band gap and electrocatalytic behavior of Ga_2O_3 ceramics.

EXPERIMENTAL DETAILS

Synthesis. $Ga_{2-x}Fe_xO_3$ (GFO, $0.0 \leq x \leq 0.3$) compounds were synthesized from procured highly pure (99.99%) precursor materials, Ga_2O_3 (Sigma-Aldrich) and Fe_2O_3 (Noah Technologies Corporation), through solid-state reaction route. To synthesize GFO compounds, initially, the precursor materials Ga_2O_3 and Fe_2O_3 were weighed in a stoichiometric ratio in accordance with the desired compound. Precursor materials weighed in a stoichiometric ratio were collected in an agate mortar and homogeneously ground in the presence of an alcohol-wetting media. To obtain single-phase GFO compounds, calcination of homogeneously mixed powders was done in a muffle furnace at 1100 °C for 6 h with a ramp rate of 10 °C/min. After calcination and confirmation phase purity, calcined powders were reground to obtain ultrafine particles with narrow particle size distribution to improve the sintered density of samples. Uniaxial hydraulic press was used to prepare circular green pellets of 8 mm diameter and 1 mm thickness [load ≈ 5 ton]. Green pellets were sintered at 1200 °C for 6 h, and sintered high-dense pellets were used for further analysis.

Characterization. *X-ray Diffraction (XRD).* Rigaku Benchtop powder X-ray diffractometer (Mini Flex II) was used to confirm the phase purity and to determine the crystal structure of synthesized GFO compounds. Scanning parameters were 10−80° (2θ range), a step size of 0.02°, and a scan rate of 0.6° min^{-1}. Structural refinement of selected compositions was carried out using full prof software package.[31]

X-ray Photoelectron Spectroscopy (XPS). The XPS spectra of GFO compounds were collected employing a Kratos Axis Ultra DLD spectrometer using a high-performance Al Kα monochromatic X-ray source (1486.6 eV) and a high-resolution hemispherical analyzer. The X-ray source was set at 150 W. Emitted photoelectrons were collected using a detector, which is aligned normally to the sample surface. Data were collected in a 700 × 300 μm^2 area with a pass energy of 20 eV, which produced a full width at half-maximum of 0.59 eV for the Ag $3d_{5/2}$ core level of a reference Ag surface. Charge neutralization was obtained with low-energy electrons (<2 eV). Data were analyzed by employing Casa XPS software using Gaussian/Lorentzian (GL(30)) line shape and Shirley background correction.[32,33] Before collecting XPS spectra, sample surfaces were cleaned using an ultraviolet ozone cleaner for a duration of 5 min, and then the samples were loaded into an XPS chamber to make sure that the contaminated carbon has been removed. The binding energy (BE) of carbon (C 1s) at 284.8 eV was used as the charge reference. Survey scans were performed at pass energies of 160 eV, while high-resolution scans were carried out at a pass energy of 20 eV. Survey scans were taken over the binding energy (BE) range of 0−1200 eV. Ga 2p spectra were collected to avoid the interference of Ga 3d peaks with the O 2s peak. Estimation error was taken ±0.01 atom % for the concentration of various elements present, i.e., Ga, Fe, and O.

Spectral Selectivity-Optical Absorption. Optical absorption edge is associated with charge transfer from the valance band to conduction band, which originally depends on the overall electronic band structure of a compound. Though the X-ray diffraction analysis shows the evidence for elemental substitution in the parent phase, however, optical absorption spectra can provide deeper insights into elemental substitution in the parent phase. Hence, we have collected the absorption

DOI: 10.1021/acsomega.9b01604
ACS Omega 2020, 5, 104−112

spectra of GFO compounds using UV−vis spectrophotometer (PerkinElmer, Model: Lambda 1050). Sintered GFO pellets were employed for the measurements.

Electrocatalytic Activity Studies. To evaluate the effect of doping on the electrocatalytic activity of the doped and undoped samples, their activity toward the hydrogen evolution reaction (HER) was analyzed. For this three-electrode system, where the sample is the working electrode, Ag/AgCl is the reference electrode, and platinum is the counter electrode, it was formulated in the presence of a 0.5 M H_2SO_4 aq electrolyte. The preparation of the working electrode was done by mixing the powdered bulk samples with 80 μL of a 5 wt % Nafion 117 solution (Sigma-Aldrich) and drop-casting 20 μL of the completely mixed solution onto a freshly polished glassy carbon working electrode. Subsequently, the redox properties were studied using linear sweep voltammetry (CHI 6273E potentiostat) with a scan rate of 20 mV s^{-1} over a voltage range of 0 to −1.3 V.

RESULTS AND DISCUSSION

Structure Refinement. Phase purity of all of the synthesized GFO compounds was confirmed by X-ray diffraction (XRD) patterns. Some insightful information on the crystal structure of GFO compounds obtained from XRD experimental results has been reported elsewhere.[34] However, the purpose of the detailed XRD high-resolution scans, as well as refinement procedures, is made in this work, to better understand the Fe site occupancy and structural distortions (if any) in the parent lattice of β-Ga_2O_3. X-ray diffraction data reveal that all of the compounds were phase-pure without any secondary phases. Figure 1 represents the refined X-ray

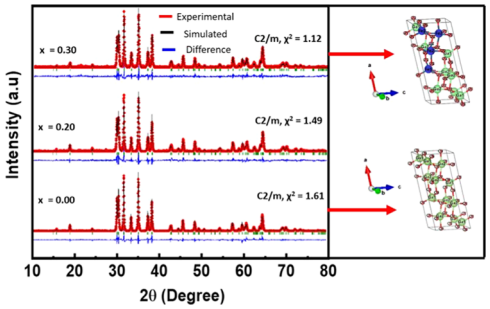

Figure 1. XRD patterns of GFO compounds. Rietveld structural refinement of XRD patterns is also presented. The experimental and calculated XRD patterns after the refinement are shown. Good agreement between the experimental and calculated XRD patterns can be noted.

diffraction patterns of selected GFO compounds. Rietveld refinement of diffraction patterns was carried out by considering the monoclinic crystal symmetry with a $C2/m$ space group. Pseudo Voigt peak shape function has been used to refine experimental diffraction patterns. In all of the refined patterns, simulated and experimental pattern intensities were fitted with a minimal differential curve. The obtained goodness of fit (χ^2) for three selected compounds is 1.61 (x = 0), 1.49 (x = 0.20), and 1.12 (x = 0.30). Hence, the structural refinement data reveals that, even at a higher concentration of Fe (x = 0.30), GFO compounds stabilize in monoclinic crystal symmetry, which is similar to the intrinsic Ga_2O_3. The refined unit cell parameters are provided in Table 1. Refined cell parameters indicate a small increment in unit cell volume

Table 1. Unit Cell Parameters of GFO Compounds Obtained from Structural Refinement

	unit cell parameters				
composition (x)	a (Å)	b (Å)	c (Å)	β (deg)	unit cell volume (Å)^3
x = 0	12.2192	3.03951	5.80541	103.856	209.341
x = 0.2	12.2555	3.04532	5.81512	103.854	210.718
x = 0.3	12.2719	3.04791	5.82019	103.811	211.402

associated with small ionic radii difference between Fe^{3+} and Ga^{3+}. The atomic coordinates obtained from the refinement procedure are listed in Table 2.

Table 2. Rietveld Structural Refinement Parameters Obtained for GFO Compounds

		atomic coordinates			
Fe concentration	atoms	X	Y	Z	U_{iso}
0.00	Ga1	0.09012	0.00000	0.79649	0.00162
	Ga2	0.15885	0.50000	0.30921	0.00471
	O1	0.15308	0.00000	0.10793	0.01013
	O2	0.17102	0.00000	0.56049	0.01013
	O3	−0.0079	0.50000	0.26514	0.01013
0.30	Ga1	0.0899	0.00000	0.7922(8)	1.00000
	Ga2	0.1577(3)	0.50000	0.3103(9)	0.01044
	O1	0.16051	0.00000	0.09246	−0.0828
	O2	0.17149	0.00000	0.56117	−0.0624
	O3	−0.00240	0.50000	0.25687	−0.0553
	Fe1	0.0899(3)	0.00000	0.7922(8)	0.00253
	Fe2	0.1577(3)	0.50000	0.3103(9)	0.00253

Electronic Structure. The XPS survey scans of GFO compounds are represented in Figure 2. The survey scans indicate core-level peaks of constituent elements such as Ga, Fe, O, Ga LMM Auger peak, O KLL, and C 1s. The C 1s peak corresponds to hydrocarbons on the surface of the samples; these hydrocarbons will form on the surface of the sample due to exposure to air before transferring the sample to an XPS chamber. However, in survey scans, we are able to observe Fe

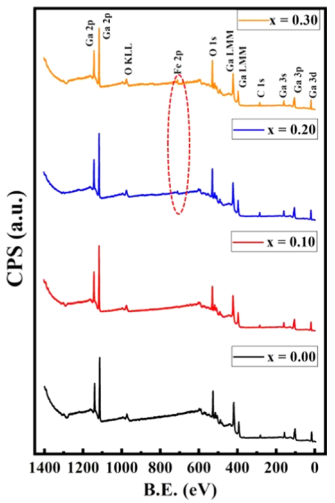

Figure 2. XPS survey scans of GFO compounds. The peaks identified are as marked.

DOI: 10.1021/acsomega.9b01604
ACS Omega 2020, 5, 104−112

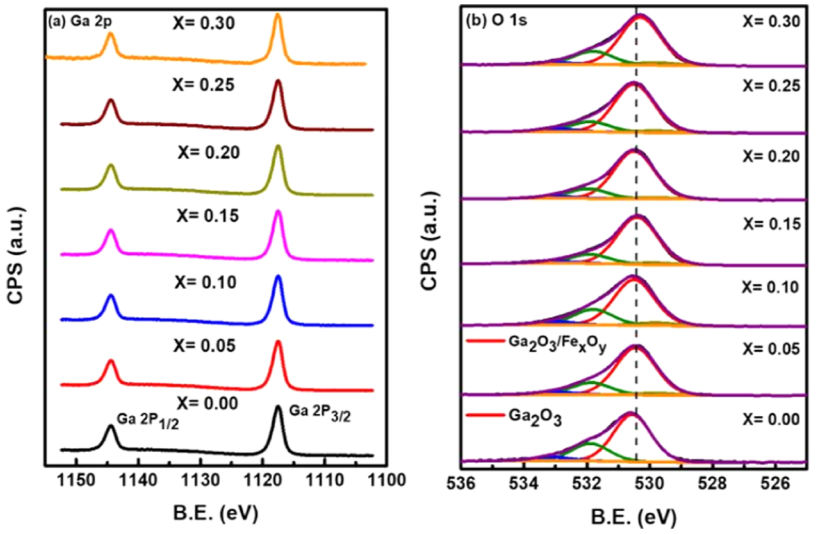

Figure 3. High-resolution XPS spectra of GFO compounds (a) Ga 2p and (b) O 1s.

3p peaks in compounds with higher Fe concentration (in Figure 2, it is indicated as a red dotted oval).

High-resolution XPS spectra of Ga 2p and O 1s peaks are shown in Figure 3. The peak assignments and binding energy (BE) comparison are made following the NIST database. The Ga 2p region (Figure 3a) shows the high-resolution spectra of both Ga $2p_{3/2}$ and Ga $2p_{1/2}$ located at ≈1117.6 and 1144.6 eV, respectively. The Ga $2p_{3/2}$ peak is located at a higher BE (1117.6 eV) in all of the GFO samples compared to pure Ga metal, which is located at 1117.0 eV.[35,36] Compared to the Ga metallic state, the observed Ga 2p core-level peaks exhibit a positive shift of 0.6 eV, indicating that all of the Ga exists in its fully oxidized state (Ga^{3+}). It has been widely reported that the Ga 2p core-level peaks exhibit a positive shift of 0.6 eV due to the redistribution of electronic charge leading to the formation of the fully oxidized state (i.e., Ga^{3+}).[37] Thus, the Ga XPS data, which are consistent with the values reported for Ga_2O_3 standard in the literature, confirms the existence of Ga ions in the highest chemical valence (Ga^{3+}). The slight change in BE and peak intensity of Ga peak with Fe doping may be due to the weakening of Ga−O bonds in Ga_2O_3. This weakening causes a decrease in the electron density around the Ga ions.[38]

The O 1s peak (Figure 3b) appears at a BE of 530 eV, which is a characteristic of Ga−O bond. This peak is very sensitive to the variation in chemical bonding.[39] It can be noted that this O 1s peak is not symmetric for all of the GFO samples. The peak fitting of the O 1s core-level peak results in at least two components representing the different chemical states or differently bonded oxygen. The most intense and main component, which is centered at a BE of 530.4 eV, is the characteristic of oxygen bonded to Ga within the GFO compound. The O 1s peak for Fe_2O_3 and/or FeO becomes merged with the O 1s peak for Ga_2O_3 as most metal-oxide peaks can be obtained in a BE range of 530−531 eV. This has caused the O 1s peaks to become slightly broader in the Fe-containing compounds. A second component, which appears as a shoulder contribution with minor intensity, is located at a higher BE of 532 eV. This component with minor intensity can be attributed to either carbonyl (oxygen bonded to carbon) or hydroxyl (oxygen bonded to hydrogen) groups, which were adsorbed onto the surface during sample handling.[36]

Figure 4 represents the high-resolution XPS spectra of Fe 2p. The deconvoluted spectra of Fe $2p_{3/2}$ peak clearly reveal that

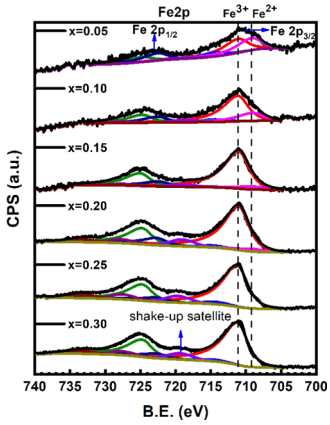

Figure 4. Deconvoluted high-resolution XPS spectra of Fe 2p of GFO compounds.

Fe exhibits mixed valance state (Fe^{3+} and Fe^{2+}) in GFO samples with lower Fe content, whereas Fe exhibits single valance state (Fe^{3+}) in compounds with higher Fe content. It is mainly because of three reasons, namely, considerable iron content, to maintain the stoichiometry, and charge neutrality. With an increasing iron concentration in the GFO compounds, the intensity of Fe peak increases, whereas the intensity of the Ga peak decreases gradually. In addition, the shake-up satellite peak around 720 eV was observed in accordance with the literature, which is the characteristic feature of Fe^{3+} in α-Fe_2O_3.[40,41] However, the satellite peak is less pronounced in compounds with mixed valency state.

Optical Properties. The optical absorption spectra and associated data analyses of GFO compounds are presented in Figure 5. It is evident from the optical absorption spectra (Figure 5a) that the Fe doping induces a change in the absorption edge. From the cutoff wavelengths of all of the compounds, it is evident that the GFO compounds with Fe concertation $x \leq 0.10$ exhibit the absorption edge in the UV regions (≤400 nm), whereas compounds with Fe concentration $x \geq 0.15$ exhibit the absorption edge in the visible

DOI: 10.1021/acsomega.9b01604
ACS Omega 2020, 5, 104−112

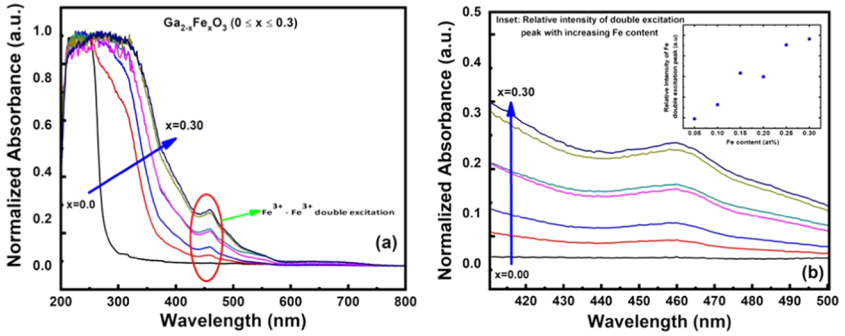

Figure 5. (a) Optical absorption spectra of GFO. (b) Enlarged profile representing the intensity variation of peak associated with Fe^{3+}–Fe^{3+} double-excitation process (inset: relative intensity of Fe-induced double-excitation edge vs Fe content).

region (≥400 nm). As the concentration of Fe increases, the absorption edge shifts from the UV to visible region, which is referred to as "red shift". In all of the GFO compounds, the progressive shift in the absorption edge is clearly noted. Moreover, a small absorption edge at ≈450 nm was found in Fe-substituted compounds (indicated with a red oval in Figure 5a). Such small absorption band is associated with a double-excitation process of Fe^{3+}–Fe^{3+} and is due to transitions from $^6A_1(S) + {}^6A_2(S)$ to $^4T_1(G) + {}^4T_2(G)$.[42−44] Figure 5b represents the enlarged profile of Fe-induced double-excitation process. The inset in Figure 5b represents the relative intensity of Fe-induced absorption edge associated with a double-excitation process with Fe concentration. From the inset figure, it is evident that the relative intensity of Fe peak increases with increasing Fe content, as expected.

Figure 6 shows the variation in the band gap of GFO compounds with Fe concentration. The determination of the cutoff wavelength to calculate the band gap is presented in the inset of Figure 4b. The band gap of intrinsic Ga_2O_3 is 4.56 (±0.01) eV, which is in good agreement with that reported in the literature.[45] However, Fe incorporation into Ga_2O_3 considerably decreases the band gap even at a very initial concentration. At the very first step of Fe, i.e., x = 0.05, the GFO compounds experience a significant reduction in band gap from 4.56 to 3.34 eV (Figure 4b). However, further doping of Fe still induces the band-gap narrowing but at a much lower rate. Overall, the band gap finally reduces to 2.95 (±0.01) eV when Fe content is increased to x = 0.30. While such a reduction in band gap is also noted in Cu-, W-, Mo-, and Ti-doped Ga_2O_3, the red shift observed in these GFO compounds even for a lower content of Fe is very significant.

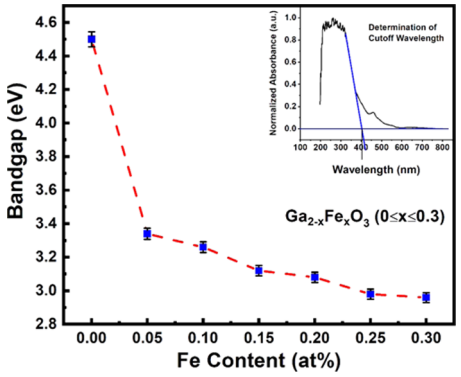

Figure 6. Band-gap variation with Fe content. Significant reduction in band gap in GFO compounds is evident.

The chemistry behind the observed wide-range spectral selectivity and red-shift band gap in GFO compounds can be explained as follows. Based on the XRD data and refinement procedure, the substitutional nature of Fe in Ga_2O_3 is evident for the entire range of dopant composition. This can be easily understood from the considerations of the Shannon ionic radii of Ga and Fe. The ionic radii of Ga and Fe are in excellent close match with each other: Ga^{3+}, 0.62 Å (octahedral coordination) and 0.47 Å (tetrahedral coordination); and Fe^{3+}, 0.64 Å (octahedral coordination) and 0.49 Å (tetrahedral coordination).[46] Therefore, Fe^{3+}can be substituted in the Ga site, which can replace Ga^{3+} from both octahedral and tetrahedral positions in stoichiometric proportion. Thus, no perturbation to the parent crystal structure, i.e., monoclinic structure of β-Ga_2O_3, is seen even at the highest concentration (x = 0.30) of Fe doping into Ga_2O_3. Under such isostructural configuration, electronic structural changes occur due to the Fe substituting for Ga. Thus, the substantial red shift observed in band gap can be explained based on the sp−d exchange interaction between valance band electrons and localized d electrons of Fe in Ga_2O_3. The sp−d exchange interactions led to positive and negative corrections to valance and conduction bands; as a consequence, band-gap narrowing occurs in the systems with sp−d exchange interactions.[47−49] In the present case, the outer-most electron configurations of Ga^{3+} and Fe^{3+} are $3d^{10}$ and $3d^5$, respectively. Therefore, in intrinsic Ga_2O_3, 3d electrons do not involve in hybridization, whereas in the case of Fe-doped Ga_2O_3 compounds, $3d^5$ electrons involve in hybridization with O p-orbitals. Owing to this, there is a strong s−d and p−d exchange interactions present in GFO compounds, which leads to abrupt band-gap narrowing. These interactions and, hence, the spectral selectivity and band gap can be tuned by carefully controlling the Fe content and, hence, the dopant chemistry in GFO compounds.

Figure 7 represents the schematic energy diagram of intrinsic β-Ga_2O_3- and Fe^{3+}-doped Ga_2O_3. The figure clearly shows positive and negative corrections to the valance band and conduction band due to sp−d exchange interaction in Fe^{3+}-doped Ga_2O_3, associated band-gap narrowing. As explained, in the case of intrinsic β-Ga_2O_3, valance band edge is dominated by O 2p orbitals and conduction band is dominated by Ga 4s orbitals, whereas in the case of Fe^{3+}-doped compounds, valance band edge is dominated by O 2p orbitals and conduction band edge is dominated by Ga 4s and Fe 3d in contrast to intrinsic β-Ga_2O_3. The sp−d exchange originates in Fe-doped compounds due to the contribution of Fe 3d electrons to conduction band.

DOI: 10.1021/acsomega.9b01604
ACS Omega 2020, 5, 104−112

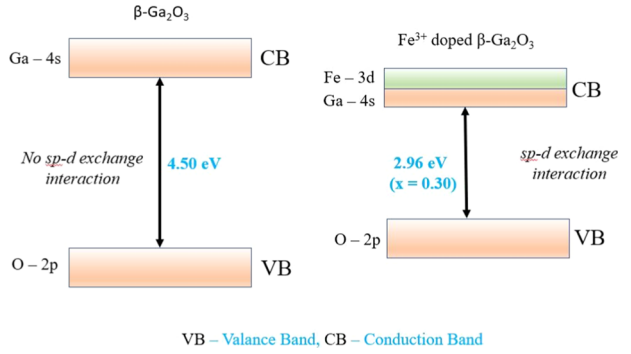

Figure 7. Schematic energy diagram of intrinsic and Fe-doped Ga_2O_3.

Electrocatalytic Activity. After confirming that Fe doping in GFO can intimately modulate its optical properties and band gap, we explored its potential to elicit unconventional properties in Ga_2O_3. While the use of Ga_2O_3 for lasers,[50] phosphors,[51] etc. is being explored in detail, its potential as a catalyst is comparatively less explored. Recent studies indicate that Ga_2O_3 has considerable utility as photocatalysts for the creation of H_2 fuel, especially through water splitting.[52] However, owing to the large band gap of Ga_2O_3 that makes electrocatalytic reactions tedious, the applicability of Ga_2O_3-based materials toward electrocatalytic processes remained unexplored. Optical band-gap analysis of GFO compounds reveals that there is significant reduction in optical band gap, which could also impact its electrocatalytic characteristics. Figure 8a,b illustrates the electrocatalytic analysis of intrinsic Ga_2O_3 and two doped samples with Fe contents 0.15 and 0.30, employing HER as the model reaction. To the best of our knowledge, Ga_2O_3-based samples (individually) as an electrocatalyst for HER are still not reported in the literature. As expected, the parent Ga_2O_3 sample did not exhibit any electrocatalytic activity under aerobic conditions within the potential range explored in the study. However, both the doped samples (GFO) demonstrated appreciable electrocatalytic activity toward the generation of H_2 through electrocatalytic water splitting (Figure 8a). Moreover, the doping percentages demonstrated an intricate relationship to the observed catalytic activity (Figure 8a,b). The GFO sample with lower doping concentration (0.15) demonstrated superior catalytic activity compared to GFO with 0.30 Fe doping (Figure 8a). GFO sample with $x = 0.15$ has an onset potential of ∼900 mV and a Tafel slope of 210 mV dec^{-1}, whereas the GFO with $x = 0.3$ showed an onset of 1036 mV and a Tafel slope of 290 mV dec^{-1} (Figure 8a,b). Three principal steps involved in the conversion of H^+ to H_2 are commonly expressed as the Volmer (eq 1), Heyrovsky (eq 2), and Tafel (eq 3) equations

Volmer:

$$H^+ + e = H_{ads}\ (\text{adsorption process}) \quad (1)$$

Heyrovsky:

$$H_{ads} + H^+ + e = H_2\ (\text{electrochemical desorption process}) \quad (2)$$

Tafel:

$$H_{ads} + H_{ads} = H_2\ (\text{recombination process}) \quad (3)$$

The high value of the Tafel slope for GFO samples reveals that the process is mostly governed through the Volmer–Heyrovsky mechanism. The inset of Figure 8a demonstrates the enlarged view of selected potential range showing the onset potential for each sample. The lower-onset potential and Tafel slope, in combination with a higher current density, revealed the superiority of 0.15 GFO sample and also emphasize the importance of ideal doping content to get enhanced catalytic activity. The electrocatalytic generation of H_2 demonstrated here proves for the first time that simple doping can evoke novel electrocatalytic performances in Ga_2O_3-based material systems.

We believe that the inculcation and modulation of electrocatalytic activity in traditionally noncatalytic Ga_2O_3 samples through Fe doping are the result of three disparate mechanisms. While it is trivial to mention that the creation of new catalytic centers in Ga_2O_3 through Fe is the reason for the electrocatalytic performance, the nonlinear and bell-shaped behavior of catalytic activity points to a more complex enabling mechanism. It is reported that transition-metal doping adjacent to catalytic centers (mostly electronegative elements such as oxygen or sulfur) in electrocatalysts can enhance its activity by lowering the hydrogen adsorption free energy (ΔG_H).[53−55] Hence, the lattice inclusion of Fe while doping creates highly catalytic centers and lowers hydrogen adsorption free energy (ΔG_H) by weakening the bonds between Ga and O atoms in the lattice, resulting in a more favorable adsorption of proton and its subsequent reduction to H_2. However, this still does not explain the modulation of catalytic activity with respect to doping content, as well as the bell-shaped behavior of the activity. The dependence of electron mobility and conductivity of the sample on catalyst performance in HER is well demonstrated. A higher electron mobility and conductivity will allow the generated electrons to travel across the catalyst

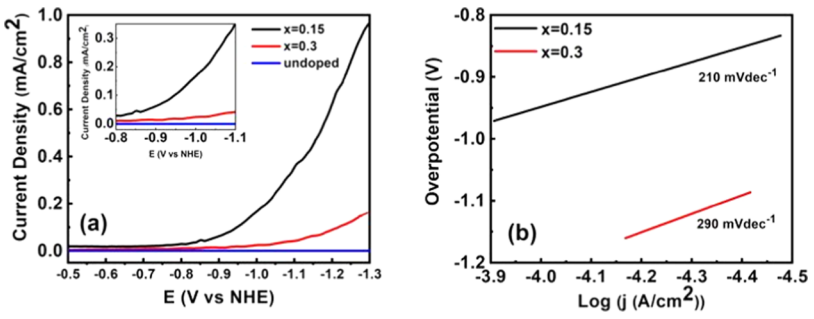

Figure 8. Electrochemical characterization of the doped and undoped Ga_2O_3. (a) Polarization curves obtained at a 20 mV s^{-1} scan rate and (b) Tafel slopes for $x = 0.15$- and 0.30-doped samples.

DOI: 10.1021/acsomega.9b01604
ACS Omega 2020, 5, 104−112

to reach the active centers to enable faster reduction, which results in lower-onset potential. The presence of metals in the sample is expected to minimally raise the conductivity values of the doped samples. However, the enhanced conductivity does not seem to follow a linear relationship with doping. From the XPS study (Figure 4), it is established that lower doping concentration of Fe has two valence states of +2 and +3, whereas the higher one has Fe only in the +3 oxidation state. The presence of Fe in mixed valence states can impart enhanced conductivity and electron mobility within the system via intervalence charge transfer.[56] Hence, between GFO sample (0.15 and 0.3), owing to the presence of mixed valence states of Fe, the O.15 GFO sample has the highest conductivity and hence demonstrates better activity. In addition to decreasing the ΔG_H value and increasing the conductivity, Fe doping also decreases the band gap of the material. Based on the observed catalytic activity, we hypothesize that the band positions (especially the conduction band) for doped samples are such that proton reduction is easier for the lower doping concentrations (illustrated in Figure 9). Hence, as a cumulative effect of the above-stated three phenomena, GFO samples with a 0.15 Fe content demonstrate the best catalytic activity toward HER.

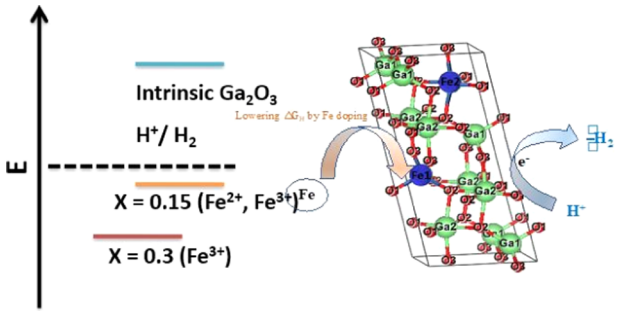

Figure 9. Hypothetical schematic showing the band positions in the conduction band for intrinsic and Fe-doped compounds.

Though we were able to inculcate appreciable electrocatalytic activity in Ga_2O_3 through simple metal doping, it is worth noting that the obtained results are not optimal for their application as an efficient electrocatalyst. However, the aim of the study was to create a new avenue for Ga_2O_3-based material in electrocatalysis and to prove that doping-induced band-gap tuning can be an effective pathway to generate tunable electrocatalytic activity in a system that had no activity in the pristine state. We postulate that engineering the doping concentration, doping type, the size and shape, inducing more catalytic centers, or creating high activity hybrids, etc. can result in Ga_2O_3-based catalyst with significantly embellished catalytic properties. However, such optimizations are beyond the scope of this work, and efforts in this direction are currently being undertaken.

SUMMARY AND CONCLUSIONS

In conclusion, Fe-doped Ga_2O_3 compounds (GFO) ($0.0 \leq x \leq 0.3$) were synthesized and their structural, chemical, optical, and electrocatalytic properties were evaluated. GFO compounds are single phase even at higher Fe concentration; structural analyses confirm that these GFO compounds crystallize in monoclinic crystal symmetry with a $C2/m$ space group. Chemical analyses indicate high-quality GFO materials, where Fe exhibits mixed chemical valence states (Fe^{3+}, Fe^{2+}) for a lower concentration of Fe doping. However, for doping with higher Fe ($x = 0.20-0.30$) content, iron ions exhibit only the single chemical valence state (Fe^{3+}). Significant red shift of the optical band gap occurs in GFO compounds compared to that in intrinsic Ga oxide. Iron-doping-facilitated strong sp−d exchange interaction, which originates from the $3d^5$ electrons of Fe^{3+}, is accounted for the observed red shift in the GFO compounds. In addition, a signature of $Fe^{3+}-Fe^{3+}$ double-excitation process is evident as a small optical absorption edge at ≈450 nm in GFO compounds. Moreover, GFO compounds (x = 0, 0.15, and 0.30) exhibit electrocatalytic water splitting toward the generation of H_2 in contrast to intrinsic Ga_2O_3. An onset potential and Tafel slope of GFO samples include: x = 0.15 (onset potential ∼900 mV and Tafel slope ∼ 210 mV dec^{-1}) and x = 0.30 (onset potential ∼1036 mV and a Tafel slope ∼290 mV dec^{-1}). The electrocatalytic activity of Fe-doped compounds was attributed to resulted new catalytic centers, enhanced conductivity, and electron mobility. As a concluding and general remark, for the first time, we explored a new pathway of deriving electrocatalytic behavior in Fe-doped Ga_2O_3, while such activity was totally absent in the intrinsic or undoped phase. Therefore, the outcomes and implications derived from this work may be applicable to a large class of compounds, and further options may be available to design functional materials for electrocatalytic energy production.

AUTHOR INFORMATION

Corresponding Author

*E-mail: rvchintalapalle@utep.edu.

ORCID

Saptasree Bose: 0000-0002-3189-5236
Sreeprasad Sreenivasan: 0000-0002-5728-0512
Vaithiyalingam Shutthanandan: 0000-0003-2957-7535
Chintalapalle V. Ramana: 0000-0002-5286-3065

Notes

The authors declare no competing financial interest.

ACKNOWLEDGMENTS

The authors acknowledge, with pleasure, support from the National Science Foundation (NSF) with NSF-PREM Grant #DMR-1827745. A portion of the research was performed using Environmental Molecular Sciences Laboratory (EMSL), a national scientific user facility sponsored by the Department of Energy's Office of Biological and Environmental Research and located at Pacific Northwest National Laboratory.

REFERENCES

(1) Pearton, S. J.; Yang, J.; Cary, P. H.; Ren, F.; Kim, J.; Tadjer, J. M.; Mastro, M. A. A review of Ga_2O_3 materials, processing, and devices. *Appl. Phys. Rev.* **2018**, *5*, No. 011301.
(2) Wenckstern, H. V. Group-III Sesquioxides: Growth, Physical Properties and Devices. *Adv. Electron. Mater.* **2017**, *3*, No. 1600350.
(3) Cui, S.; Mei, Z.; Zhang, Y.; Liang, H.; Du, X. Room-Temperature Fabricated Amorphous Ga_2O_3 High-Response-Speed Solar-Blind Photodetector on Rigid and Flexible Substrates. *Adv. Opt. Mater.* **2017**, *5*, No. 1700454.
(4) Muhammed, M. M.; Alwadai, N.; Lopatin, S.; Kuramata, A.; Roqan, I. S. High-Efficiency InGaN/GaN Quantum Well-Based Vertical Light-Emitting Diodes Fabricated on β-Ga_2O_3 Substrate. *ACS Appl. Mater. Interfaces* **2017**, *9*, 34057−34063.
(5) Carey, B. J.; Ou, J. Z.; Clark, R. M.; Berean, K. J.; Zavabeti, A.; Chesman, A. S. R.; Russo, S. P.; Lau, D. W. M.; Xu, Z. Q.; Bao, Q.;

DOI: 10.1021/acsomega.9b01604
ACS Omega 2020, 5, 104−112

Kavehei, O.; Gibson, B. C.; Dickey, M. D.; Kaner, R. B.; Daeneke, T.; Zadeh, K. K. Wafer-scale two-dimensional semiconductors from printed oxide skin of liquid metals. *Nat. Commun.* **2017**, *8*, No. 14482.
(6) Ghose, S.; Rahman, S.; Hong, L.; Rojas-Ramirez, J. S.; Jin, H.; Park, K.; Klie, R.; Droopad, R. Growth and characterization of β-Ga_2O_3 thin films by molecular beam epitaxy for deep-UV photodetectors. *J. Appl. Phys.* **2017**, *122*, No. 095302.
(7) Oleksak, R. P.; Stickle, W. F.; Herman, G. S. Aqueous-based synthesis of gallium tungsten oxide thin film dielectrics. *J. Mater. Chem. C* **2015**, *3*, 3114−3120.
(8) Dong, L.; Jia, R.; Xin, B.; Peng, B.; Zhang, Y. Effects of oxygen vacancies on the structural and optical properties of β-Ga_2O_3. *Sci. Rep.* **2017**, *7*, No. 40160.
(9) Fleischer, M.; Haurierder, W.; Meixner, H. Stability of semiconducting Gallium Oxide Thin Films. *Thin Solid Films* **1990**, *190*, 93−102.
(10) Lin, H. J.; Gao, H.; Gao, P. X. UV-enhanced CO sensing using Ga_2O_3-based nanorod arrays at elevated temperature. *Appl. Phys. Lett.* **2017**, *110*, 043101−043105.
(11) Lin, H. J.; Baltrus, J. P.; Gao, H.; Ding, Y.; Nam, C. Y.; Ohodnicki, P.; Gao, P. X. Perovskite Nanoparticle-Sensitized Ga_2O_3 Nanorod Arrays for CO Detection at High Temperature. *ACS Appl. Mater. Interfaces* **2016**, *8*, 8880−8887.
(12) Mazeina, L.; Perkins, F. K.; Bermudez, V. M.; Arnold, S. P.; Prokes, S. M. Functionalized Ga2O3 Nanowires as Active Material in Room Temperature Capacitance-Based Gas Sensors. *Langmuir* **2010**, *26*, 13722−13726.
(13) Ogita, M.; Saika, N.; Nakanishi, Y.; Hatanaka, Y. Ga_2O_3 thin films for high-temperature gas sensors. *Appl. Surf. Sci.* **2001**, *175*−*176*, 721−725.
(14) Ogita, M.; Saika, N.; Nakanishi, Y.; Hatanaka, Y. Ga_2O_3 thin films for high-temperature gas sensors. *Appl. Surf. Sci.* **1999**, *142*, 188−191.
(15) Bartic, M.; Baban, C.; Suzuki, H.; Ogita, M.; Isai, M. β-Gallium Oxide as Oxygen Gas Sensors at a High Temperature. *J. Am. Ceram. Soc.* **2007**, *90*, 2879−2884.
(16) Yang, G.; Jang, S.; Ren, F.; Pearton, S. J.; Kim, J. Influence of high-energy proton irradiation on β-Ga_2O_3 nanobelt field-effect transistors. *ACS Appl. Mater. Interfaces* **2017**, *9*, 40471−40476.
(17) Aubay, E.; D. Gourier, D. Magnetic bistability and Overhauser shift of conduction electrons in gallium oxide. *Phys. Rev. B* **1993**, *47*, 15023−15036.
(18) Binet, L.; Gourier, D. Bistable Magnetic Resonance of Conduction Electrons in Solids. *J. Phys. Chem. A* **1996**, *100*, 17630−17639.
(19) Kroll, P.; Dronskowski, R.; M. Martin, M. Formation of spinel-type gallium oxynitrides: a density-functional study of binary and ternary phases in the system Ga−O−N. *J. Mater. Chem.* **2005**, *15*, 3296−3302.
(20) Åhman, J.; Svensson, G.; Albertson, J. A reinvestigation of β − gallium oxide. *Acta. Crystallogr., Sect. C: Cryst. Struct. Commun.* **1996**, *52*, 1336−1338.
(21) Rafique, S.; Han, L.; Tadjer, M. J.; Freitas, J. A., Jr.; Mahadik, N. A.; Zhao, H. Homoepitaxial growth of β-Ga_2O_3 thin films by low pressure chemical vapor deposition. *Appl. Phys. Lett.* **2016**, *108*, 182105.
(22) López, I.; Nogales, E.; Méndez, B.; Piqueras, J.; Peche, A.; Ramírez-Castellanos, J.; González-Calbet, J. M. Influence of Sn and Cr Doping on Morphology and Luminescence of Thermally Grown Ga_2O_3 Nanowires. *J. Phys. Chem. C* **2013**, *117*, 3036−3045.
(23) Wang, X.; Shen, S.; Jin, S.; Yang, J.; Li, M.; Wang, X.; Han, H.; Li, C. Effects of Zn^{2+} and Pb^{2+} dopants on the activity of Ga_2O_3-based photocatalysts for water splitting. *Phys. Chem. Chem. Phys.* **2013**, *15*, 19380−19386.
(24) Sakata, Y.; Matsuda, Y.; Yanagida, T.; Hirata, K.; Imamura, H.; Teramura, K. Effect of Metal Ion Addition in a Ni Supported Ga_2O_3 Photocatalyst on the Photocatalytic Overall Splitting of H_2O. *Catal. Lett.* **2008**, *125*, 22−26.
(25) Zhang, W.; Naidu, B. S.; Ou, J. Z.; O'Mullane, A. P.; Chrimes, A. F.; Carey, B. J.; Wang, Y.; Tang, S. Y.; Sivan, V.; Mitchell, A.; Bhargava, S. K.; Kalantar-zadeh, K. Liquid Metal/Metal Oxide Frameworks with Incorporated Ga_2O_3 for Photocatalysis. *ACS Appl. Mater. Interfaces* **2015**, *7*, 1943−1948.
(26) Syed, N.; Zavabeti, A.; Mohiuddin, M.; Zhang, B.; Wang, Y.; Datta, R. S.; Paul Atkin, P.; Carey, B. J.; Tan, C.; Embden, J. V.; Chesman, A. S. R.; Ou, J. Z.; Daeneke, T.; Zadeh, K. K. Sonication-Assisted Synthesis of Gallium Oxide Suspensions Featuring Trap State Absorption: Test of Photochemistry. *Adv. Funct. Mater.* **2017**, *27*, No. 1702295.
(27) Battu, A. K.; Manandhar, S.; Shutthanandan, V.; Ramana, C. V. Controlled optical properties via chemical composition tuning in molybdenum-incorporated β-Ga_2O_3 nanocrystalline films. *Chem. Phys. Lett.* **2017**, *684*, 363−367.
(28) Zhang, Y.; Yan, J.; Li, Q.; Qu, C.; Zhang, L.; Xie, W. Optical and structural properties of Cu-doped Ga_2O_3 films. *Mater. Sci. Eng., B* **2011**, *176*, 846−849.
(29) Rubio, E. J.; C. V. Ramana, C. V. Tungsten-incorporation induced red-shift in the bandgap of gallium oxide thin films. *Appl. Phys. Lett.* **2013**, *102*, No. 191913.
(30) Manandhar, S.; Ramana, C. V. Direct, functional relationship between structural and optical properties in titanium-incorporated gallium oxide nanocrystalline thin films. *Appl. Phys. Lett.* **2017**, *110*, No. 061902.
(31) Rodríguez-Carvajal, J. Recent advances in magnetic structure determination neutron powder diffraction. *Phys. B* **1993**, *192*, 55−69.
(32) Fairley, N.; Carrick, A. *The Casa Cookbook Part 1: Recipes for XPS Data Processing*; Acolyte Science, 2005.
(33) Végh, J. Comments on "A study of amorphous Ti−Ni alloys by X-ray photoelectron spectroscopy". *J. Electron Spectrosc. Relat. Phenom.* **2006**, *151*, 155−157.
(34) Roy, S.; Mallesham, B.; Zade, V. B.; Martinez, A.; Shutthanandan, V.; Thevuthasan, S.; Ramana, C. V. Correlation between Structure, Chemistry, and Dielectric Properties of Iron-Doped Gallium Oxide ($Ga_{2-x}Fe_xO_3$). *J. Phys. Chem. C* **2018**, *122*, 27597−27607.
(35) Rubio, E. J.; Mates, T. E.; Manandhar, S.; Nandasiri, M.; Shutthanandan, V.; Ramana, C. V. Tungsten Incorporation into Gallium Oxide: Crystal Structure, Surface and Interface Chemistry, Thermal Stability, and Interdiffusion. *J. Phys. Chem. C* **2016**, *120*, 26720−26735.
(36) Ramana, C. V.; Rubio, E. J.; Barraza, C. D.; Gallardo, M.; McPeak, S.; Kotru, S.; Grant, J. T. Chemical bonding, optical constants, and electrical resistivity of sputter-deposited gallium oxide thin films. *J. Appl. Phys.* **2014**, *115*, No. 043508.
(37) López, I.; Utrilla, A. D.; Nogales, E.; Mendez, B.; Piqueras, J.; Peche, A.; Ramirez-Castellano; Gonzalez-Cabelt, J. M. In-Doped Gallium Oxide Micro- and Nanostructures: Morphology, Structure, and Luminescence Properties. *J. Phys. Chem. C* **2012**, *116*, 3935−3943.
(38) Patil, S. B.; Kim, I. Y.; Gunjakar, J. L.; Oh, S. M.; Eom, T.; Kim, H.; Hwang, S. J. Phase Tuning of Nanostructured Gallium Oxide via Hybridization with Reduced Graphene Oxide for Superior Anode Performance in Li- Ion Battery: An Experimental and Theoretical Study. *ACS Appl. Mater. Interfaces* **2015**, *7*, 18679−18688.
(39) López, I.; Orts, M. A.; Nogales, E.; Méndez, B.; Piqueras, J. Influence of Li doping on the morphology and luminescence of Ga_2O_3 microrods grown by a vapor-solid method. *Semicond. Sci. Technol.* **2016**, *31*, No. 115003.
(40) Kraushofer, F.; Jakub, Z.; Bichler, M.; Hulva, J.; Drmota, P.; Weinold, M.; Schmid, M.; Setvin, M.; Diebold, U.; Blaha, P.; Parkinson, G. S. Atomic-Scale Structure of the Hematite α-$Fe_2O_3(1\bar{1}02)$ "R-Cut". *J. Phys. Chem. C* **2018**, *122*, 1657−1669.
(41) Hu, X.; Yu, J. C.; Gong, J.; Li, Q.; Li, G. α-Fe_2O_3 Nanorings Prepared by a Microwave-Assisted Hydrothermal Process and Their Sensing Properties. *Adv. Mater.* **2007**, *19*, 2324−2329.
(42) He, Y. P.; Miao, Y. M.; Li, C. R.; Wang, S. Q.; Cao, L.; Xie, S. S.; Yang, G. Z.; Zou, B. S. Size and structure effect on optical

DOI: 10.1021/acsomega.9b01604
ACS Omega 2020, 5, 104−112

transitions of iron oxide nanocrystals. *Phys. Rev. B* **2005**, *71*, 125411−125419.
(43) Hashimoto, T.; Yamada, T.; Yoko, T. Third-order nonlinear optical properties of sol−gel derived α-Fe_2O_3, γ-Fe_2O_3, and Fe_3O_4 thin films. *J. Appl. Phys.* **1996**, *80*, 3184−3190.
(44) Toloman, D.; Popa, A.; Stan, M.; Silipas, T. D.; Biris, A. R. Identification of Different Iron Sites in β-Ga_2O_3 Nanoparticles by Spectroscopic Methods. *AIP Conf. Proc.* **2015**, *1700*, No. 060005.
(45) Onuma, T.; Saito, S.; Sasaki, K.; Masui, T.; Yamaguchi, T.; Honda, T.; Higashiwaki, M. Valence band ordering in β-Ga_2O_3 studied by polarized transmittance and reflectance spectroscopy. *Jpn. J. Appl. Phys.* **2015**, *54*, No. 112601.
(46) Shannon, R. D. Revised effective ionic radii and systematic studies of interatomic distances in halides and chalcogenides. *Acta Crystallogr., Sect. A* **1976**, *32*, 751−767.
(47) Bouaine, A.; Brihi, N.; Schmerber, G.; Ulhaq-Bouillet, C.; Colis, S.; Dinia, A. Structural, Optical, and Magnetic Properties of Co-doped SnO_2 Powders Synthesized by the Coprecipitation Technique. *J. Phys. Chem. C* **2007**, *111*, 2924−2928.
(48) Li, Y. W.; Sun, J. L.; Meng, X. J.; Chu, J. H.; Zhang, W. F. Structural and optical properties of $Ba(Co_x,Ti_{1-x})O_3$ thin films fabricated by sol-gel process. *Appl. Phys. Lett.* **2004**, *85*, 1964−1966.
(49) Stroud, D.; Ehrenreich, H. Band structure of SiGe: Coherent-potential approximation. *Phys. Rev. B* **1970**, *2*, 3197−3209.
(50) Mu, W.; Yin, Y.; Jia, Z.; Wang, L.; Sun, J.; Wang, M.; Tang, C.; Hu, Q.; Gao, Z.; Zhang, J.; Lin, N.; Veronesi, S.; Wang, Z.; Zhao, X.; Tao, X. An extended application of β-Ga_2O_3 single crystals to the laser field: Cr^{4+}:β-Ga_2O_3 utilized as a new promising saturable absorber. *RSC Adv.* **2017**, *7*, 21815−21819.
(51) Tamura, T.; Setomoto, T.; Taguchi, T. Illumination characteristics of lighting array using 10 candela-class white LEDs under AC 100 V operation. *J. Lumin.* **2000**, *87*−*89*, 1180−1183.
(52) Li, X.; Zhen, X.; Meng, S.; Xian, J.; Shao, Y.; Fu, X.; Li, D. Structuring β-Ga_2O_3 Photonic Crystal Photocatalyst for Efficient Degradation of Organic Pollutants. *Environ. Sci. Technol.* **2013**, *47*, 9911−9917.
(53) Escalera-López, D.; Niu, Y.; Yin, J.; Cooke, K.; Rees, N. V.; Palmer, R. E. Enhancement of the Hydrogen Evolution Reaction from Ni-MoS_2 Hybrid Nanoclusters. *ACS Catal.* **2016**, *6*, 6008−6017.
(54) Hota, P.; Bose, S.; Dinda, D.; Das, P.; Ghorai, U. K.; Bag, S.; Mondal, S.; Saha, S. K. Nickel-Doped Silver Sulfide: An Efficient Air-Stable Electrocatalyst for Hydrogen Evolution from Neutral Water. *ACS Omega* **2018**, *3*, 17070−17076.
(55) Shi, Y.; Zhou, Y.; Yang, D. R.; Xu, W. X.; Wang, C.; Wang, F. B.; Xu, J. J.; Xia, X. H.; H. Chen, H. Y. Energy Level Engineering of MoS_2 by Transition-Metal Doping for Accelerating Hydrogen Evolution Reaction. *J. Am. Chem. Soc.* **2017**, *139*, 15479−15485.
(56) Park, J. G.; Aubrey, M. L.; Oktawiec, J.; Chakarawet, K.; Darago, L. E.; Grandjean, F.; G. Long, G. J.; Long, J. R. Charge Delocalization and Bulk Electronic Conductivity in the Mixed-Valence Metal−Organic Framework $Fe(1,2,3\text{-triazolate})_2(BF_4)_x$. *J. Am. Chem. Soc.* **2018**, *140*, 8526−8534.

DOI: 10.1021/acsomega.9b01604
ACS Omega 2020, 5, 104−112